nature energy

Article

https://doi.org/10.1038/s41560-025-01883-w

Recoverable operation strategy for selective and stable electrochemical carbon dioxide reduction to methane

Received: 23 December 2024

Accepted: 10 September 2025

Published online: 16 October 2025

Check for updates

Guorui Gao[1,8], Behnam Nourmohammadi Khiarak[1,8], Hengzhou Liu[2,8], Thành Trần-Phú[3], Cornelius A. Obasanjo[1], Jackson Crane[4], Hung D. T. Lai[1], Gelson T. S. T. da Silva[1,5], Viktoria Golovanova[6], Jiantao Li[2], Huajie Ze[2], John Weiss[2], Zedong Zhang[2], Sungsik Lee[7], Rosalie K. Hocking[3], F. Pelayo García de Arquer[6], Edward H. Sargent[2] ✉ & Cao-Thang Dinh[1] ✉

In the carbon dioxide (CO_2) electroreduction reaction, catalysts determine, to a large extent, the system's product selectivity, energy efficiency and stability. Conventionally, catalysts are prepared and optimized ex situ before the reaction, but they often suffer from low stability due to intrinsic structural changes during the reaction. Here we demonstrate a recoverable operation strategy for selective and stable electroreduction of CO_2 to methane. In this approach, active catalysts are formed and fully reset in situ during CO_2 electroreduction reaction. By stabilizing catalyst precursors and controlling the formation and removal of the catalysts, we demonstrate an over 500-hour CO_2-to-methane conversion with a Faradaic efficiency of over 60% at the reduction current density of above 0.2 A cm^{-2} and full-cell voltage of below 4.0 V. We further showcase benefits of the recoverable operation for potential integration with intermittent renewable power supply, contributing to more than 100 days with day-on and night-off operation.

The electrochemical carbon dioxide (CO_2) reduction reaction (CO_2RR) to valuable chemicals driven by renewable energy can contribute to achieving net-zero emissions[1,2]. Among the various products electro-synthesized using CO_2RR, methane (CH_4) stands out in terms of its high energy density (55.5 MJ kg^{-1}) (ref. 3), which is important for energy storage applications. The seamless compatibility with existing gas infrastructure, including transportation pipelines and storage facilities, makes it suited for large-scale and long-term energy storage. Compared to thermocatalytic methanation, CO_2RR has the advantage of integration, modular scalability and bypasses the requirement for external steady hydrogen (H_2) sources[4,5]. In addition, the ability of electrochemical reactors to ramp up and down quickly makes them more compatible with intermittent renewable sources compared to thermocatalytic processes[6,7].

In CO_2RR, and more broadly, in electrosynthesis, catalysts are employed to enhance the reaction rate and selectivity of chemical transformations[8]. Commonly, catalysts are developed based on tuned composition, structure, morphology and surface function to address specific reaction intermediates and improve rates[9,10]. These strategies aim to regulate key factors that govern the CO_2RR

[1]Department of Chemical Engineering, Queen's University, Kingston, Ontario, Canada. [2]Department of Chemistry, Northwestern University, Evanston, IL, USA. [3]School of Science, Computing and Emerging Technologies, Swinburne University of Technology, Melbourne, Victoria, Australia. [4]Department of Mechanical and Materials Engineering, Queen's University, Kingston, Ontario, Canada. [5]Interdisciplinary Laboratory of Electrochemistry and Ceramics, Department of Chemistry, Federal University of Sao Carlos, São Carlos, Brazil. [6]ICFO–Institut de Ciències Fotòniques, The Barcelona Institute of Science and Technology, Barcelona, Spain. [7]X-ray Science Division, Argonne National Laboratory, Lemont, IL, USA. [8]These authors contributed equally: Guorui Gao, Behnam Nourmohammadi Khiarak, Hengzhou Liu. ✉e-mail: ted.sargent@northwestern.edu; caothang.dinh@queensu.ca

https://doi.org/10.1038/s41560-025-01883-w

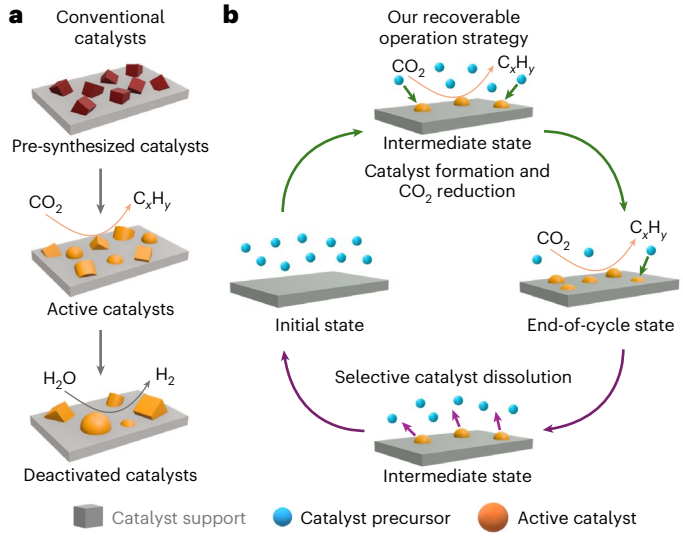

Fig. 1 | Schematic illustration of the CO_2 to hydrocarbon conversion process using different strategies. a, Conventional steady-state approach using pre-synthesized catalysts. The pre-synthesized catalysts change during CO_2RR, leading to the formation of deactivated catalysts, which often produce H_2 as the main product. **b**, Proposed 'recoverable operation' approach on in situ prepared Cu catalysts. Active catalysts are formed during the CO_2RR process from the catalyst precursor in the electrolyte solution. At the end of each cycle, the catalysts are selectively removed from the substrate, forming the initial state to complete a cycle.

process, including active sites and the local reaction environment on the catalyst surface.

The practical viability of CO_2 conversion hinges on catalysts that combine high selectivity, commercially relevant current densities and extended durability—a challenge that has yet to be fully met. This is largely due to the dynamic character of electrocatalysts: catalysts dissolve, reconstruct and deactivate over time, which affects interaction with reactive species. In CO_2RR, this typically promotes the undesired hydrogen evolution reaction (HER)[11,12] (Fig. 1a). For copper (Cu)-based catalysts, which are often used for CO_2 conversion to hydrocarbons and alcohols, such structural evolution during CO_2RR has been frequently observed[13–15]. In addition to their instability during CO_2RR, Cu-based catalysts also undergo structural changes when the reaction is not under the operating reducing potential, making it challenging to integrate CO_2RR with intermittent renewable energy sources[16,17]. Beyond Cu, similar transformations are common on noble metal catalysts, including gold and palladium, for CO_2RR to carbon monoxide (CO)[18].

Common strategies to enhance catalyst stability include alloying[19,20], element decoration[21,22], core-shell confinement[23,24] and additive tuning[25,26], among others[27,28]. For example, alloying Cu with antimony and palladium was suggested to improve catalyst stability by lowering surface energy[29]. Core-shell structures have been reported to stabilize the oxidation state and enhance the surface adhesion energy of the Cu nanocrystals by a hybrid organic/inorganic alumina shell[30]. Despite noticeable progress, the lifetime of reported catalysts remains limited to the hundreds of hours[31] and typically only to a few hours at application-relevant (>0.2 A cm^{-2}) high-reduction-current densities[26,32,33].

We argue that these strategies, based on modifying Cu-based (pre)catalysts, may slow down reconstruction processes but still face a fundamental performance-durability trade-off. Therefore, instead of relying on conventional ex situ pre-catalyst compositional and structural tuning, we report a strategy based on recoverable operation, where catalysts are in situ synthesized and fully reset during electrochemical operation to overcome this intrinsic limitation (Fig. 1b). The repetition of the cycle enables selective and long-term CO_2RR to hydrocarbons (C_xH_y). Utilizing a membrane electrode assembly (MEA) cell with dissolved CO_2 feed, we achieved a methane Faradaic efficiency (FE) exceeding 60% at reduction current densities above 0.2 A cm^{-2}. The system maintained CH_4 production for over 500 hours at a full-cell voltage of 4.0 V. Furthermore, the system showed adaptability to intermittent renewable energy sources and fluctuating power supply, with over 100 days of operation under an alternating day-on/night-off cycle.

Validation of the recoverable operation concept

To test the feasibility of the recoverable operation concept, we first performed the CO_2RR in an H-cell with 0.3 M potassium bicarbonate ($KHCO_3$) at the cathode, saturated with CO_2 and containing 3.6 ppm Cu^{2+}. The electrolysis was conducted with electrodeposition of Cu onto the silver (Ag) mesh substrate at cathodic potential, followed by dissolution of Cu to Cu^{2+} at anodic potential (Fig. 2a). The oxidation potential (+0.25 V vs Ag/AgCl) for Cu dissolution was selected based on the cyclic voltammetry curves (Supplementary Note 1).

We first investigated the effect of Cu deposition on CO_2RR performance by adjusting the deposition/dissolution (Re/Ox) times for 5 s/5 s, 60 s/60 s, 120 s/120 s and 180 s/180 s at various reduction potentials (−2.2, −3.1 and −3.9 V vs Ag/AgCl). Under different reduction potentials, 5 s/5 s of Cu deposition/dissolution time consistently showed the highest CO_2 reduction selectivity (Fig. 2b and Supplementary Fig. 2). When increasing the applied cathodic potential from −2.2 to −3.1 V vs Ag/AgCl, the FE for CH_4 was improved significantly from ~17% to ~47%, whereas the FE for CO decreased from ~41% to ~17%. Further increase in applied potential did not increase CH_4 selectivity but promoted HER. A series of control experiments, including reactions using bare Ag mesh and Cu mesh, suggests that the freshly formed Cu-based catalysts originating from free Cu^{2+} ions in the electrolyte served as the active catalysts for CH_4 production (Supplementary Note 2). We also validated the FE values by examining the Cu redox processes under pulsed electrolysis, and we concluded that the Cu reduction contributed negligibly (<0.5%) to the experimentally obtained FE (Supplementary Note 3).

To evaluate the possible benefits and any limitations of fabricated catalysts under recoverable operation compared to pre-synthesized catalysts, we first performed alternated −3.1 V vs Ag/AgCl for 120 s and +0.25 V vs Ag/AgCl for 120 s of Re/Ox electrolysis using an electrolyte containing 3.6 ppm Cu^{2+} precursor (Supplementary Fig. 7). The results showed that a stable production of CH_4 with over 45% FE was obtained for 1,800 s of operation. At the end of the 2,040 s (after a 120-s Cu deposition), we refreshed the electrolyte to eliminate the Cu^{2+} ions and set a constant potential. Notably, the selectivity of CH_4 dropped dramatically, with the HER becoming the dominant reaction, which means that the recoverable strategy is necessary to maintain the selective and stable catalysts.

We employed ex situ synchrotron-radiation-based X-ray absorption spectroscopy (XAS) to analyse the coordination structures of Cu species after electroreduction treatment (120 s). The Cu K-edge X-ray absorption near-edge structure (XANES) spectra and fitting result show that the absorption edge is between that of metallic Cu and Cu_2O[34,35] (Fig. 2c and Supplementary Fig. 8), which corresponds with the characteristic peaks of metallic Cu and Cu_2O in extended X-ray absorption fine structure (EXAFS) spectra (Fig. 2d), with no detectable Cu(II) species. X-ray photoelectron spectroscopy (XPS) analyses further confirmed these findings as only Cu^0 and Cu^+ are detected (Supplementary Fig. 9a). The XPS survey spectra (Fig. 2e and Supplementary Note 4) and scanning electron microscopy-energy dispersive spectroscopy (SEM-EDS) (Fig. 2f and Supplementary Note 5) taken on samples after oxidation and reduction cycles reveal recoverable changes in both surface elemental composition and morphology. The observed dynamic changes in Cu signals prove the formation and dissolution of active Cu particles after reduction and oxidation steps, respectively.

https://doi.org/10.1038/s41560-025-01883-w

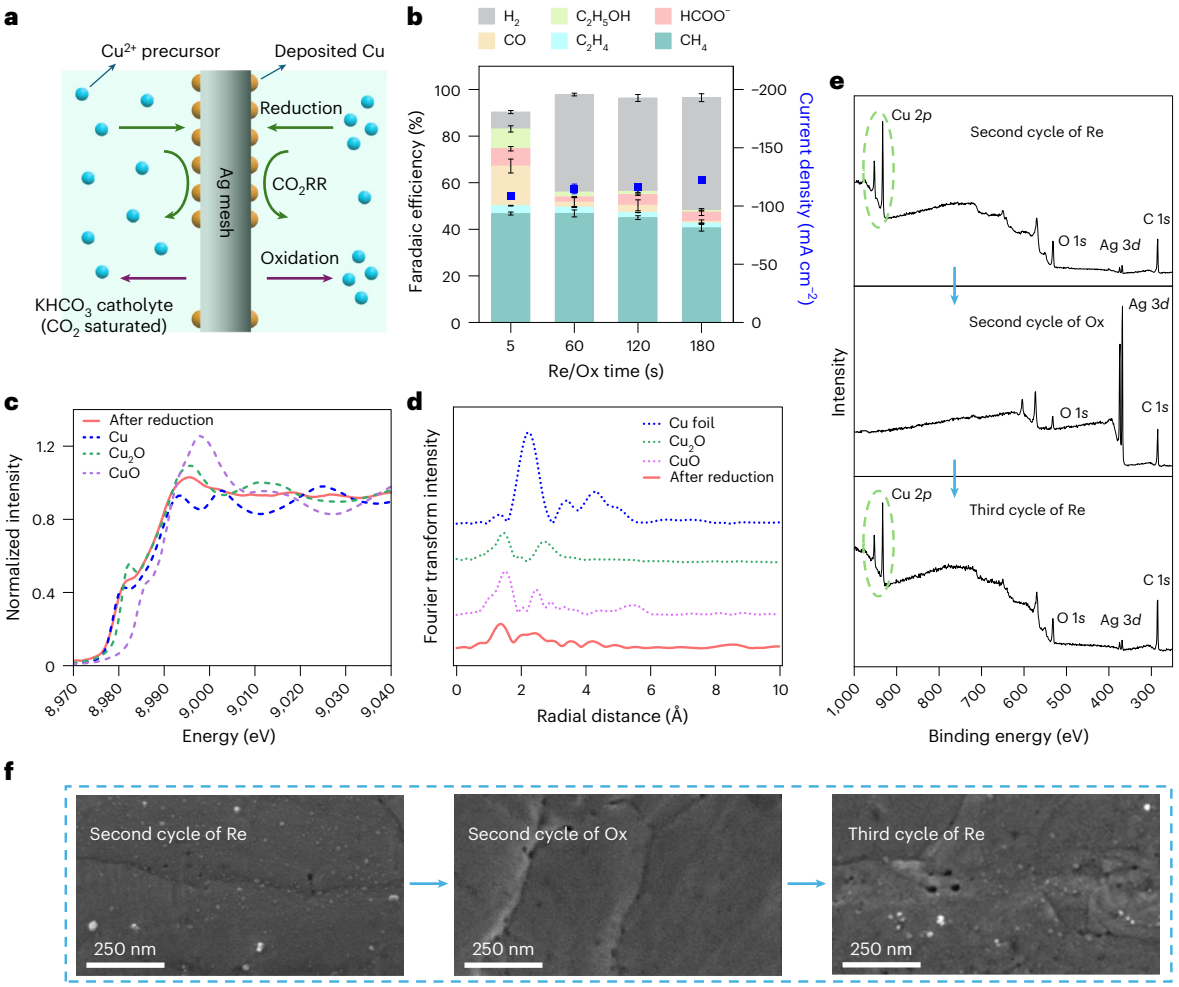

Fig. 2 | Proof of concept of the recoverable operation in a conventional H-cell configuration. a, Schematic representation of the 'recoverable operation' strategy using an Ag substrate and Cu active catalysts. **b**, System optimization using 5 s/5 s, 60 s/60 s, 120 s/120 s and 180 s/180 s of reduction and oxidation (Re/Ox) times, respectively, and at a reduction potential of −3.1 V versus Ag/AgCl and an oxidation potential of +0.25 V versus Ag/AgCl. Error bars represent the standard deviation (SD) of measurements based on three independent trials. Data are presented as mean values ± SD. **c**,**d**, Cu K-edge XANES (**c**) and corresponding Fourier-transformed (FT)-EXAFS spectra of post-Cu deposition electrode after 120-s reduction at the potential of −3.1 V versus Ag/AgCl (**d**). Dashed lines represent reference components. **e**, XPS survey spectra of post-reaction electrode after 120-s Cu deposition or dissolution at the reduction potential of −3.1 V versus Ag/AgCl or the oxidation potential of +0.25 V versus Ag/AgCl. **f**, SEM images of corresponding electrodes from XPS analyses. Scattered nanoparticle spots were found after the reduction treatment.

To characterize the dynamic structure changes of Cu-based active sites during electrolysis, we performed in situ Raman and XAS analyses. At an open-circuit potential and at −1.8 V vs Ag/AgCl, without Cu^{2+} in the electrolyte, no significant Raman peaks were observed (Fig. 3a). Upon addition of Cu^{2+}, peaks for different reaction intermediates appeared at the negative potential between −0.2 and −1.8 V versus Ag/AgCl[36–38], but no peaks were related to Cu_2O and CuO, indicating the metallic state of Cu-based active sites at reduction potentials. Notably, at potentials more negative than −0.2 V vs Ag/AgCl, peaks associated with CH_4 formation intermediates, such as linearly adsorbed CO and C–H stretching vibrations, were detectable. As the potential was further scanned to 0 V vs Ag/AgCl, two distinct peaks appeared at 519 and 631 cm^{-1}, corresponding to vibrational modes of Cu_2O[37], with no signals for CuO. When the potential shifted more positively (Fig. 3b), the intensity of these Cu_2O peaks gradually diminished and disappeared, which means the oxidative dissolution of surface Cu species from the Ag substrate into the electrolyte. Further analysis by holding the potential at +0.1 V vs Ag/AgCl up to 1,200 s revealed the dynamic formation and disappearance of Cu_2O species (Fig. 3c), indicating the gradual dissolution of surface Cu_2O, consistent with our pulsed electrolysis strategy for controllable Cu deposition and dissolution.

In situ XAS results show a substantial shift between Cu-based catalyst formation and removal within the first three cycles of pulsed Re/Ox electrolysis (Fig. 3d–f). During the reduction period, Cu^{2+} from the electrolyte electrodeposited on the substrate and mainly formed metallic Cu, which was subsequently oxidized and dissolved back to the electrolyte (Supplementary Figs. 19–21). By fixing the energy at the rising edge (8,985 eV) and applying a pulsed potential (10 s) between −1.0 and +0.25 V versus Ag/AgCl, the dynamic change in Cu^{2+} fluorescence intensity inside the electrolyte was observed, and the result revealed a reversible process between the deposition of Cu^{2+} from the electrolyte and its dissolution back to the electrolyte (Supplementary Fig. 22). These observations demonstrate the high recoverability of the Cu-based active sites during pulsed electrolysis.

Recoverable operation strategy at high currents

To test the recoverable operation concept at high current densities, we performed CO_2RR in a MEA cell coupled with a bipolar membrane (BPM) (Fig. 4a and Supplementary Fig. 23). The catholyte, composed of 0.3 M

https://doi.org/10.1038/s41560-025-01883-w

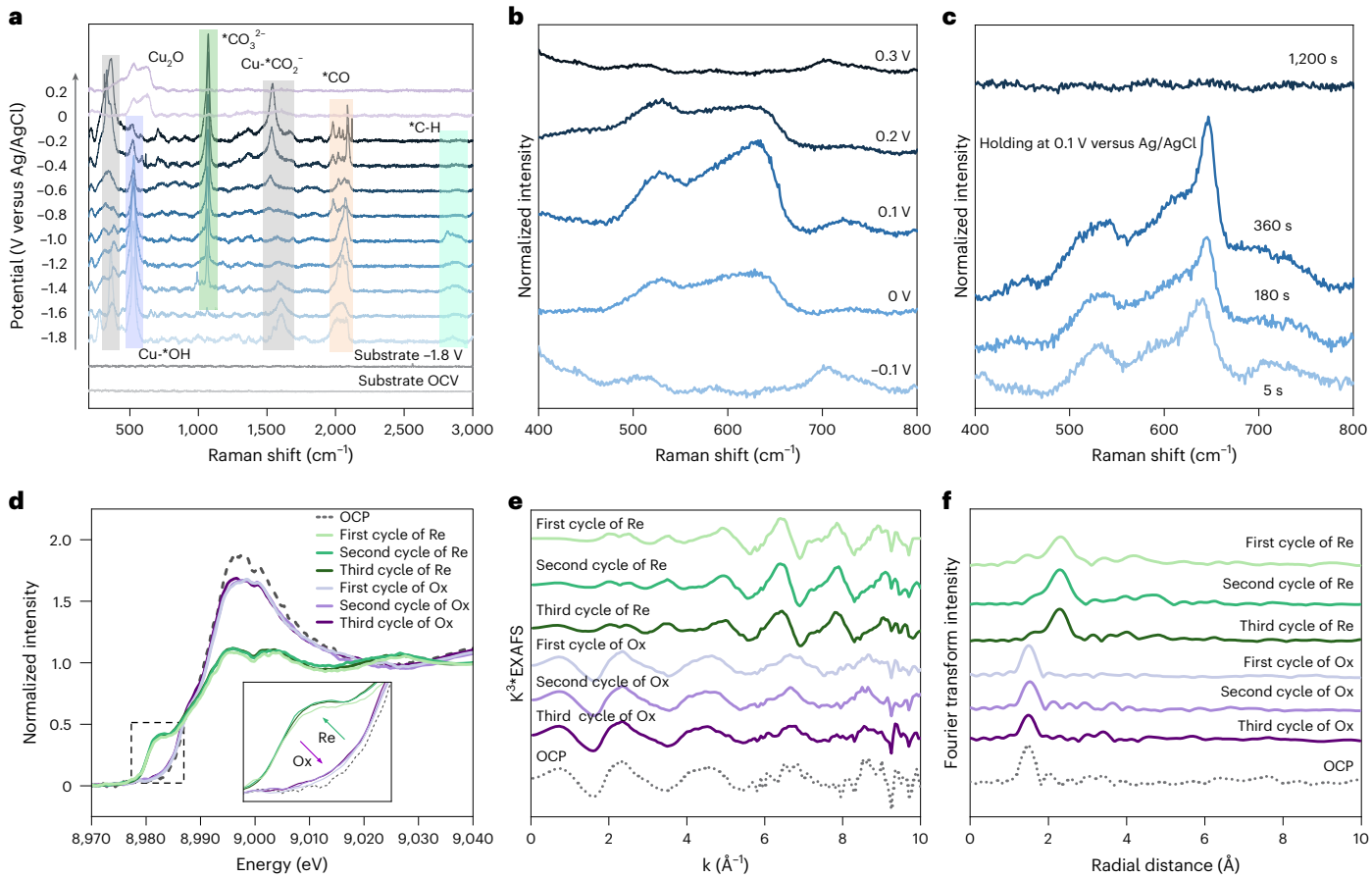

Fig. 3 | In situ characterization of the catalysts under recoverable operation. **a**, Potential-dependent Raman spectra in the CO_2-saturated 0.3 M $KHCO_3$ containing 3.6 ppm Cu^{2+}, showing development of adsorbed components and reaction intermediates. OCV, open-circuit voltage. **b**, Potential-dependent Raman spectra illustrating the dynamic change and removal of deposited Cu-based catalysts at the evaluated positive potential. **c**, Time-dependent Raman spectra showing the dynamic change and removal of deposited Cu-based catalysts by holding the oxidation potential at +0.1 V versus Ag/AgCl. **d**–**f**, In situ X-ray absorption spectroscopy: Cu K-edge XANES (**d**), corresponding EXAFS (**e**) and FT-EXAFS spectra (**f**) in the CO_2-saturated 0.3 M $KHCO_3$ containing 3.6 ppm Cu^{2+}, showing the dynamic changes between Cu deposition (first cycle, second cycle and third cycle at −1.0 V versus Ag/AgCl) and dissolution (first cycle, second cycle and third cycle at +0.25 V versus Ag/AgCl) under pulsed electrolysis for three cycles. The inset in panel **d** is a zoomed-in figure from energy of 8,978 eV to 8,987 eV. The dashed line for open-circuit potential (OCP) represents the characteristic of Cu^{2+} ions in the electrolyte.

$KHCO_3$, with dissolved CO_2 and Cu^{2+}, was circulated through the cathode compartment. Ag meshes, identical to those used in the H-cell tests, were used as the cathode. Ni foam and 1 M potassium hydroxide (KOH) solution were used as anode and anolyte, respectively. All CO_2RR tests with BPM were performed by alternating cell voltages between an oxidation voltage of −1.0 V and a CO_2 reduction voltage in the range of −4.5 to −8.0 V (Supplementary Note 6). Unless stated otherwise, oxidation and reduction times were fixed at 5 s/5 s, because these conditions yielded the highest C_xH_y:H_2 ratio in the H-cell tests (Supplementary Fig. 26).

In our cell configuration, CO_2 reactant comes from two sources, one of CO_2 dissolved in bulk electrolyte (Supplementary Fig. 27a) and the other of in situ regenerated CO_2 from the reaction between bicarbonate ions and protons from the BPM (Supplementary Fig. 27b,c)[39,40]. As a result, higher CO_2RR partial current densities can be achieved when compared to those using either dissolved or in situ generated CO_2 sources alone (Supplementary Fig. 27c). We also simulated the limiting current density for CH_4 production in a configuration with in situ CO_2 only (argon (Ar)-saturated in Fig. 4b) and with both CO_2 sources active (CO_2-saturated in Fig. 4b). The theoretically maximum current density for CH_4 production with both CO_2 sources exceeds our experimental results under the highest applied cell voltage, suggesting that the CO_2 availability is sufficient for high current density operation in our system (Supplementary Fig. 27c).

We then explored the effect of Cu^{2+} concentration in the catholyte and found that it did not significantly influence the cell voltages. A current density range of −100 to −500 mA cm^{-2} was attained with applied potential from −4.5 to −8.0 V at all Cu^{2+} concentrations from 0.5 to 28.8 ppm (Fig. 4c and Supplementary Fig. 28). However, the Cu^{2+} concentrations greatly affected product distribution. At a low Cu^{2+} concentration of 0.5 ppm, CO was the main gaseous CO_2RR product at a low current range, but the hydrocarbons became the dominant gaseous products of CO_2RR as the Cu^{2+} concentration increased. Remarkably, current densities exceeding −450 mA cm^{-2} can be achieved in the CO_2-limited aqueous system with a CH_4 selectivity of over 60% (for 3.6-ppm and 14.4-ppm conditions), demonstrating the high activity of the recoverable operation for CO_2RR.

On the basis of these, we selected a 3.6 ppm Cu^{2+} concentration to investigate the stability in the BPM-MEA system based on the highest C_xH_y:H_2 ratio (Supplementary Fig. 29). The system showed a starting CH_4 FE of 66% but gradually decreased to 28% after a 130-hour operation (Fig. 4d and Supplementary Fig. 30). From the modelling results (Supplementary Fig. 31a), a high local alkaline environment (maximum pH of ~12) was observed across the electrode at the current density of −250 mA cm^{-2}. We subsequently evaluated the stability of Cu^{2+} in electrolytes with different pH values, and we observed that Cu^{2+} was stable in CO_2-saturated $KHCO_3$ (pH of 7) but precipitated at a pH of 12

https://doi.org/10.1038/s41560-025-01883-w

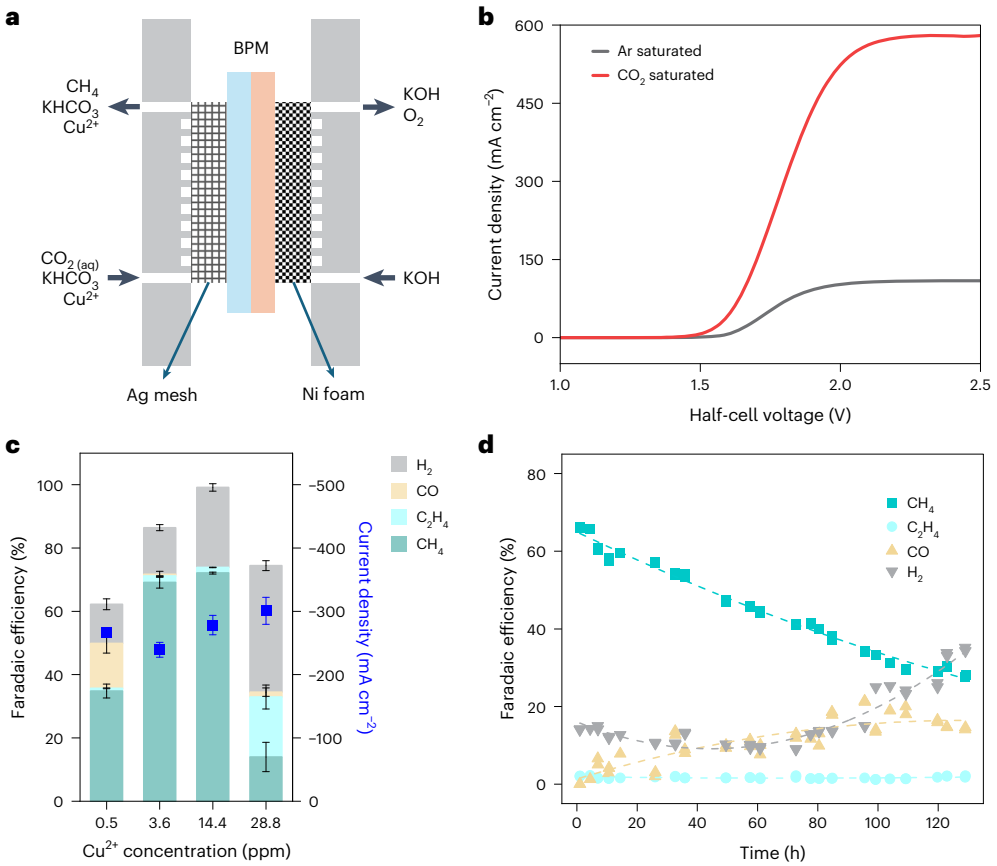

Fig. 4 | Performance demonstration in a BPM-MEA cell configuration. **a**, Schematic representation of the BPM-MEA cell employed in this study (from right to left: anode flow plate, anode nickel foam catalyst, bipolar membrane, Ag mesh substrate, cathode flow plate). 'aq' represents 'aqueous'; '$CO_{2\,(aq)}$' represents 'CO_2 dissolved in the solution'. **b**, Simulated limiting current density of CH_4 production with 0.3 M $KHCO_3$ under Ar or CO_2 sparging as a function of cathode half-cell voltage. **c**, Effect of Cu^{2+} concentration on CH_4 product selectivity at the reduction voltage of −6.0 V and the oxidation voltage of −1.0 V. Reduction/oxidation time of 5 s/5 s was used. Error bars represent the SD of measurements based on three independent trials. Data are presented as mean values ± SD. **d**, Stability performance of the BPM-MEA system operated with oxidation voltage of −1.0 V and a reduction voltage to maintain current density over −200 mA cm^{-2} using 3.6 ppm Cu^{2+} concentration. The fitted lines through the data points are guides to the eye.

(Supplementary Fig. 31b). We thus attributed the performance degradation to the continuous loss of Cu species during the long-term test, with evidence of an increase in the CO production over time (Fig. 4c,d). Within the period of the reduction process, OH^- ions were formed around the electrode by CO_2RR and HER. When the potential was turned to anodic, deposited Cu species were oxidized to Cu^{2+}, and a part of Cu^{2+} ions were prone to form $Cu(OH)_2$ by combining with OH^- locally[41], which decomposed to Cu_xO_y gradually (Supplementary Fig. 32). These compounds were insoluble in water and tended to adhere to the flow channel and the outlet tube when they were carried out by electrolyte (Supplementary Fig. 33). Besides, results from the inductively coupled plasma-optical emission spectrometer (ICP-OES) indicated that the Cu^{2+} concentration in the catholyte was lower following the stability test as compared to the beginning, confirming that Cu^{2+} ions were lost from the bulk electrolyte over time (Supplementary Table 1).

Long-term stability with stable catalyst precursors

To address the instability of the Cu^{2+} precursor in the electrolyte during CO_2RR, we complexed pyridine (Py) with Cu (Py-Cu^{2+}) (Fig. 5a) as the Cu catalyst precursor, seeking to enable a relay-like Cu dispatch regulation effect. The sp^2 lone pair orbital of 'N' in the benzene ring overlaps with the vacant metal orbital, producing a σ bonding interaction, which makes the Py a ligand to stabilize the (Cu^{2+})[42,43]. The complex precursor exhibited good stability under an alkaline environment (pH of 12) in our simulated operation conditions (Supplementary Figs. 31a and 34). We first investigated whether the Py affects the chemical characteristics of freshly formed active sites using ex situ XPS and in situ XAS. We observed similar characteristic peaks for Cu-based active catalysts under the conditions with and without Py stabilization after reduction potential, suggesting a similar nature of the Cu active phase (Fig. 5b,c and Supplementary Figs. 35–39).

Next, we chose three different Py:Cu^{2+} molar ratios of 4:1, 20:1 and 40:1 to explore the CO_2RR performance on the MEA cell system. Adding Py did not significantly change the current–voltage behaviour of the system, but H_2 generation increased with a corresponding decrease in CH_4 production as the Py concentration increased (Fig. 5d and Supplementary Fig. 40). At higher current densities over −200 mA cm^{-2}, a CH_4 FE of over 60% was obtained for the ratios of 4:1 and 20:1. CH_4 FE decreased to ~50% when a Py:Cu^{2+} ratio of 40:1 was used.

To understand the effect of Py on the formation of active Cu catalysts, we first conducted a series of cyclic voltammetry (CV) measurements using varying Py:Cu molar ratios (Supplementary Fig. 41). We observed the decrease in the intensity of Cu oxidation peaks with increasing Py:Cu molar ratios, suggesting that the presence of Py hinders Cu deposition on the Ag surface. XPS analysis further confirmed this inhibitory effect, showing a reduced Cu:Ag ratio in the presence of Py (Supplementary Fig. 35). Linear sweep voltammetry (LSV) results indicated that the addition of Py slightly shifted the onset potential for Cu^{2+} reduction to more negative values (Supplementary Fig. 42),

https://doi.org/10.1038/s41560-025-01883-w

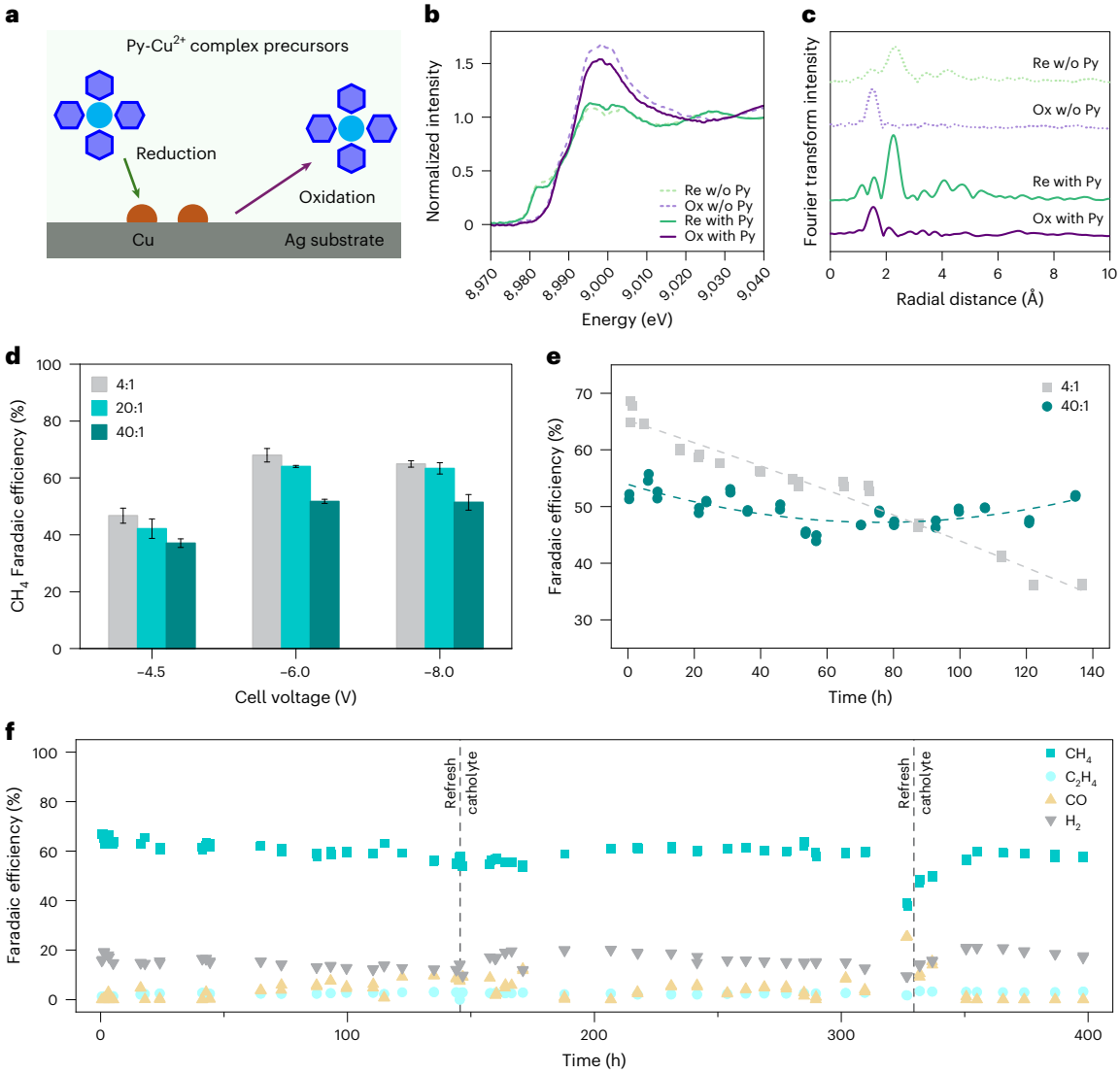

Fig. 5 | Effect of Py-Cu^{2+} complex for improved stability performance in BPM-MEA system. a, Schematic representation of the reduction and oxidation segments of Cu catalyst on an Ag mesh substrate with Py addition. **b**,**c**, In situ XAS: Cu K-edge XANES (**b**) and corresponding FT-EXAFS spectra (**c**) comparing the conditions with and without Py addition. A 300-s reduction or oxidation for each cycle was required to obtain the spectra. 'w/o' stands for 'without'. **d**, Comparison of CH_4 selectivity for different Py:Cu^{2+} molar ratios at different reduction voltages of −4.5 V, −6.0 V and −8.0 V with an oxidation voltage of −1.0 V. Error bars represent the SD of measurements based on three independent trials. Data are presented as mean values ± SD. **e**, Comparison of CH_4 product stability for Py:Cu^{2+} molar ratios of 4:1 and 40:1 throughout 130 h. The operation started with an oxidation voltage of −1.0 V and a reduction voltage of −6.0 V (and was adjusted) to maintain the current density of approximately −200 mA cm^{-2}. **f**, Gaseous product stability of the system operated with oxidation voltage of −1.0 V and a reduction voltage of −6.0 V (and was adjusted) to maintain the current density of approximately −200 mA cm^{-2} using a Py:Cu^{2+} molar ratio of 20:1. All ratios considered were based on 3.6 ppm Cu^{2+} concentration, and a reduction/oxidation time of 5 s/5 s was used for all stability tests.

reinforcing the conclusion that Py ligands hinder the reduction of Cu^{2+} cations.

To investigate the possible adsorption of Py on the catalyst surface, we conducted in situ Raman measurements in the presence of Py in the electrolyte. We observed characteristic peaks of Py at 632, 1,016, 1,213 and 1,598 cm^{-1} under negative applied potentials (Supplementary Fig. 43b)[44]. These peaks were not detectable when the applied potentials were either positive (+0.2 V) or more negative than −1.0 V, suggesting that Py adsorption on the electrode surface is potential-dependent. Our in situ Raman spectra also showed a decrease in the intensity of CO_2 reduction intermediates in the presence of Py, which could result from the reduced amount of active Cu deposited when Py is added (Supplementary Figs. 43a and 44). This observation is consistent with the LSV results, which show lower CO_2RR currents in the presence of Py in the electrolyte (Supplementary Fig. 45).

To examine whether Py adsorption can stabilize Cu catalysts for CH_4 production, we conducted a series of control experiments (Supplementary Note 7 and Supplementary Figs. 46 and 47). We first deposited Cu on an Ag mesh to produce a catalyst with high CH_4 selectivity. Then, we applied different electrolysis strategies using an electrolyte containing Py but without added Cu^{2+}. We observed that CH_4 production was not stable under either constant or pulsed potentials. These results indicate that adsorbed Py does not act as a protective layer for the active sites.

Extended durability tests were performed for all Py:Cu^{2+} molar ratios to evaluate the effect of Py on system stability, and the current density was maintained at around −200 mA cm^{-2} by adjusting the cell voltage over time. The existence of Py increased the stability of CO_2RR, but the decrease in CH_4 FE still occurred for nearly 140-hour operation at the ratio of 4:1 (Fig. 5e and Supplementary Fig. 48). However, with the

https://doi.org/10.1038/s41560-025-01883-w

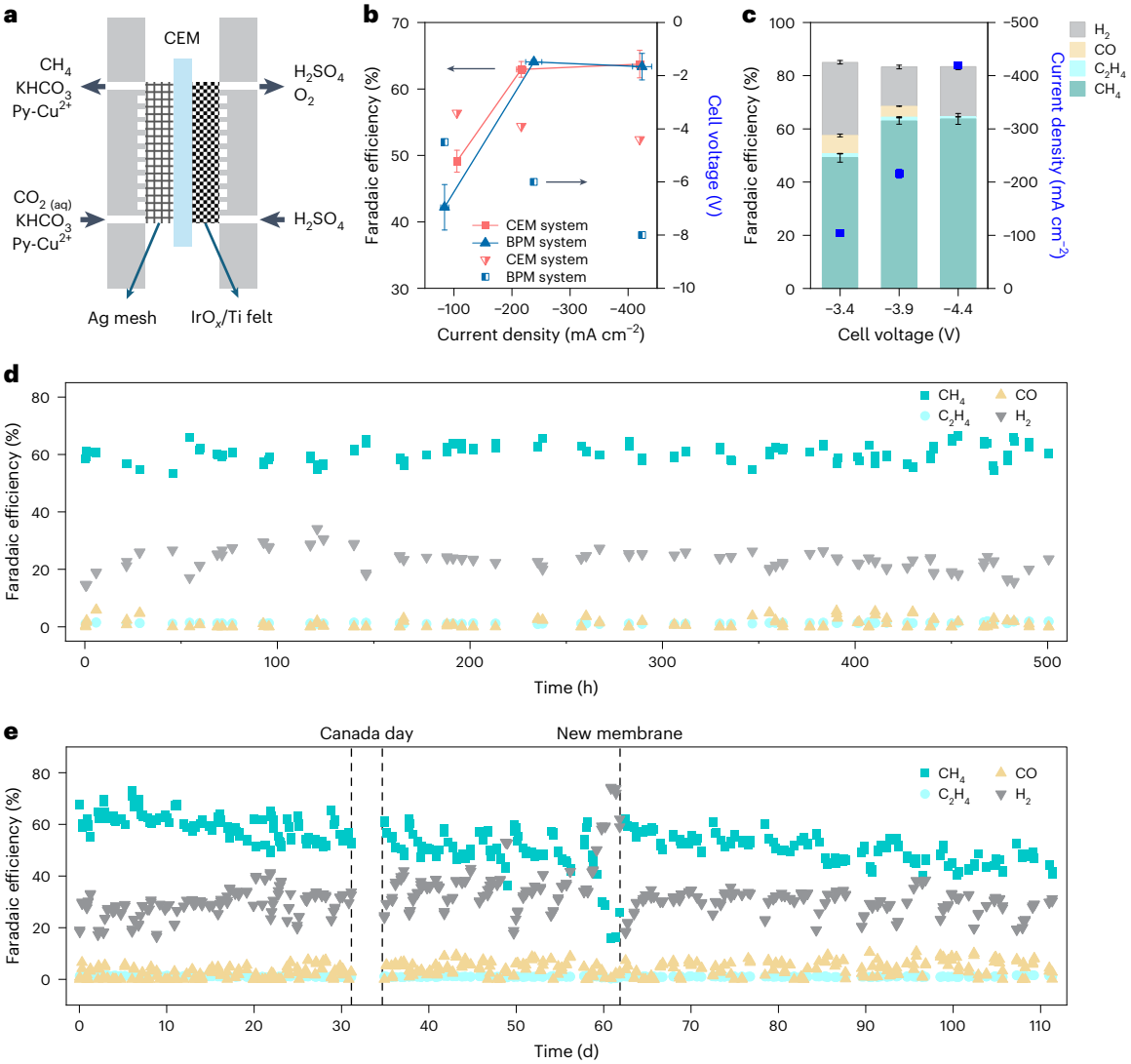

Fig. 6 | Long-term stability demonstration with improved energy efficiency in CEM-MEA system. a, Schematic representation of the CEM-MEA cell configuration employed. **b**, Reduction voltage and CH_4 selectivity performance comparison at similar current densities. **c**, Gaseous product distribution in CEM-MEA cell configuration with corresponding current densities at the cell voltages tested. An oxidation voltage of −1.1 V was used for this test. Error bars represent the SD of measurements based on three independent trials. Data are presented as mean values ± SD. **d**, Stability performance of the system operated with oxidation voltage of −1.1 V and a reduction voltage to maintain current density over −200 mA cm^{-2} using a Py:Cu^{2+} molar ratio of 20:1. Electrolytes for both cathode and anode were refreshed around every 48 hours. **e**, Intermittent operation of the system operated with oxidation voltage of −1.1 V and a reduction voltage to maintain current density over −200 mA cm^{-2} using a Py:Cu^{2+} molar ratio of 20:1. The ratio considered was based on a 3.6 ppm Cu^{2+} concentration. Electrolytes for both the cathode and anode were refreshed around every four days.

ratios of 20:1 and 40:1, significant improvements were achieved with no noticeable decline in CH_4 FE for the similar operation time (Fig. 5e,f and Supplementary Figs. 49 and 50). We used ICP-OES to quantify the Cu^{2+} concentration in the bulk electrolyte after prolonged operation with varying Py concentrations (Supplementary Table 1). The results indicate that increasing the Py concentration reduces the loss of Cu^{2+} from the electrolyte.

Improvement in energy efficiency with CEM-MEA cell configuration

Whereas MEA with BPM offers a platform for CO_2RR with high selectivity and stability, the high resistance of traditional and commercial BPM leads to high operating cell voltage and reduces the energy efficiency of CO_2RR[45,46]. To reduce cell voltage at high currents, we explored a cell configuration of MEA with a cation exchange membrane (CEM). In this system, iridium oxide (IrO_x) supported on titanium (Ti) felt and diluted sulfuric acid (0.05 M H_2SO_4) were used as anode and anolyte, respectively (Fig. 6a). In the CEM-MEA cell configuration, a reduction voltage of −3.9 V to −4.4 V was needed to achieve a current density of over −200 mA cm^{-2} to −400 mA cm^{-2}, which is 2.1 V to 3.6 V lower than those in BPM-MEA at similar current densities (Fig. 6b). The CEM-MEA system exhibited a similar product distribution to the BPM-MEA system, delivering a CH_4 FE of 60% at the current density of −210 and −420 mA cm^{-2} at reduction voltage of −3.9 and −4.4 V, respectively (Fig. 6c).

To investigate the stability of the CEM-MEA system with the recoverable operation concept, we conducted CO_2RR by cyclically alternating the voltage between −1.0 V and −3.8 V and tracking the current and products over time. We found that a stable current of around −200 mA cm^{-2} and CH_4 FE of around 60% were maintained throughout the run of 500 hours (Fig. 6d), which is remarkable compared to reported works (Supplementary Table 2). It is worth noting that the reduction voltage of this long-term operation only increased from

−3.8 V to −4.0 V compared to −6.0 V to −8.0 V for the 400-hour operation of the BPM-MEA system, demonstrating the more energy-efficient configuration (Supplementary Figs. 50 and 51).

We also evaluated the potential application of the recoverable concept in intermittent operation. To achieve this, we performed CO_2RR during the daytime for approximately 12 hours and then turned off the system at nighttime for the remainder of the time (Supplementary Fig. 52). With this intermittent mode, the system was kept operating for more than 100 days, maintaining a high CH_4 FE of 50% at a current density of over −200 mA cm^{-2} (Fig. 6e). With the recoverable operation strategy, the active sites were formed only during CO_2RR and had no effect when the system was turned off. As a result, the system can be very stable during intermittent operation and offer a promising platform for the integration of renewable but intermittent electricity and CO_2RR technology.

We also investigated the recoverable operation strategy for C_2 product generation under intermittent conditions. To produce C_2 products, we employed porous Ag mesh substrates with a high surface area[47] (Supplementary Fig. 53) and used a high concentration of Cu^{2+} in the electrolyte (36 ppm). A pulsed electrolysis programme with long reduction (20 s) and oxidation (20 s) steps was implemented. Preliminary results revealed that C_2 production with a FE of 35% was maintained for over 100 hours of intermittent operation at a current density of −120 mA cm^{-2} (Supplementary Fig. 54).

Conclusion

We report a concept of recoverable operation to extend the durability of the CO_2RR system. In our approach, Cu catalysts are periodically deposited onto the Ag substrate in situ during CO_2RR, followed by catalyst dissolution in an oxidation process before deactivation. CH_4 production at high current densities was demonstrated through the MEA cell with aqueous carbon-rich feed. By stabilizing the catalyst precursors and optimizing the cell resistance, the system delivered a CH_4 Faradaic efficiency of over 60% at a current density of over −200 mA cm^{-2} and a full-cell voltage of 4 V for a 500-hour stable operation. Operation with day-on/night-off shifts was explored to investigate the compatibility between recoverable operation and intermittent power supply, and more than 100 days of operation were realized in our system. Given the diversity of metal precursor complexes and the possibility of regulating the active sites, this approach represents a promising pathway for developing stable catalysts for a variety of electrochemical processes.

Methods

Materials

All chemicals were purchased and used as received unless otherwise noted. The bipolar membrane (BPM) (Fumasep FBM, Fuel Cell Store) and cation exchange membrane (CEM) (Aquivion E9809S, Fuel Cell Store) were utilized. The copper (Cu) mesh and silver (Ag) mesh (Amazon online store) were used as acquired without pretreatment. The carbon paper (Sigracet 39BB) was obtained from Fuel Cell Store and iridium oxide (IrO_x) coated on titanium (Ti) felt was purchased from Magneto Special Anodes. Potassium bicarbonate ($KHCO_3$, 99.9%), potassium hydroxide (KOH, 99%), sulfuric acid (H_2SO_4) and copper(II) sulfate pentahydrate ($CuSO_4 \cdot 5H_2O$) were purchased from Sigma-Aldrich. Pyridine was obtained from Sigma-Aldrich (99.8%). Argon (Ar) and carbon dioxide (CO_2) (Praxair, 99.99%) gas cylinder was used as sources for sparging and gas carrier. Ultrapure water (18.2 MΩ cm) was prepared using a Thermo Fisher Scientific water purifier. The activation of the Ag mesh was performed using cyclic voltammetry (CV) at a scan rate of 50 mV s^{-1} between +1.0 and −1.0 V (vs Ag/AgCl) for ten cycles. The activation was carried out in a two-chamber electrochemical H-cell separated by a BPM, where the cathode chamber contained 1 M $KHCO_3$ solution, and the anode chamber contained 5 M KOH. Activated Ag mesh (1 × 2 cm) was used as the working electrode, whereas a platinum mesh and an Ag/AgCl (3 M potassium chloride (KCl)) electrode served as the counter and reference electrodes, respectively.

Electrochemical CO_2 reduction

H-cell. Electrolytic measurements were performed with an Autolab PGSTAT204 potentiostat coupled with a current booster (Metrohm Autolab, 10 A). A conventional H-cell was employed in this study, which comprises a cathodic and an anodic compartment. The compartments were separated by a BPM (Fumasep) in reverse bias. Fifty ml CO_2-saturated 0.3 M $KHCO_3$ was used as the catholyte, whereas 50 ml 1 M KOH was used as the anolyte. $CuSO_4 \cdot 5H_2O$ was used as the catalyst precursor and added to the catholyte before the start of the reaction. The working electrode (Ag mesh) with an exposed surface dimension of 1 cm × 1 cm was immersed in the catholyte, facing a leak-free Ag/AgCl (3 M KCl) reference electrode. A Pt electrode served as the counter electrode in the anodic compartment. CO_2 gas was kept bubbling into the catholyte, and the catholyte was continuously stirred throughout the testing process. CV curves were carried out in an H-cell at a scan rate of 50 mV s^{-1} in CO_2-saturated 0.3 M $KHCO_3$. Linear sweeping voltammetry (LSV) curves were determined in an H-cell at a scan rate of 50 mV s^{-1} in Ar- or CO_2-saturated 0.3 M $KHCO_3$.

MEA cell

For experiments carried out in the BPM-membrane electrode assembly (MEA) cell configuration, Ag mesh (110 pores per inch (ppi)) and nickel foam (1.5 mm thickness; 80–100 ppi, MTI Corp.) were used as the cathode and anode, respectively. The compartments were separated by a BPM (Fumasep). Details of the electrolysis cell arrangement and the electrolysis system employed in this work are described in Supplementary Fig. 23. The exposed sizes of both the cathode and anode electrodes were 1 cm × 2 cm (a geometric area of 2 cm^2 was used for all current density calculations). The Ag mesh was configured to be in direct contact with the membrane. The polytetrafluoroethylene (PTFE) gasket was used to prevent contact between the anode and cathode titanium flow plates. A PTFE spacer was used to avoid direct contact between the Ag mesh and the cathode flow plate. In the CEM-MEA configuration, IrO_x/Ti felt was used as the anode, whereas a polypropylene mesh was used as the spacer that separates the cathode flow plate from the Ag mesh catalyst. For the test carried out in the BPM-MEA cell, the catholyte that was continuously stirred and circulated via the cathodic plate flow channel was 500 ml of CO_2-saturated 0.3 M $KHCO_3$. CO_2 was also continuously bubbled into the catholyte solution throughout the testing period. The anolyte circulated through the anodic flow channel was 200 ml of 1 M KOH. Similarly, for the CEM-MEA system, the catholyte and anolyte used were 500 ml of CO_2-saturated 0.3 M $KHCO_3$ and 200 ml of 0.05 M H_2SO_4, respectively. For each potential screening, the electrolysis testing was carried out with the online gas product being analysed between 2,000 s and 2,400 s.

Product analysis

The two-phase flow catholyte coming out from the cell was pumped back to the catholyte reservoir, where the gas products were accumulated and collected in the reservoir headspace. The headspace of the reservoir was connected to a manual six-way valve, which controlled the injection of accumulated gas products to the gas chromatography (GC, PerkinElmer Clarus 590) for measurements. The GC is equipped with detectors—a flame ionization detector that operates at 250 °C and a thermal conductivity detector that operates at 180 °C. Whereas a Carboxen-1000 packed column (Supelco) attached to the flame ionization detector was utilized to quantify CH_4, C_2H_4 and other possible hydrocarbons, a molecular sieve (5 A) packed column (Supelco) connected to the thermal conductivity detector was used to evaluate CO, CO_2 and H_2 products. The two columns were operated with Ar carrier gas (flow rate of 20 sccm) at a fixed temperature of 180 °C.

Aliquots of the liquid products were analysed using Nuclear Magnetic Resonance spectroscopy. Freshly obtained samples were examined on a Bruker spectrometer (400 MHz) in 10% D_2O, employing water suppression mode (PRESAT). Dimethyl sulfoxide served as the internal standard.

The Faradaic efficiency (FE) of gaseous products was calculated as follows:

$$\mathrm{FE}_i = \frac{z_i \times \mathrm{F} \times x_i \times F_\mathrm{m}}{I} \times 100\% \quad (1)$$

where FE_i is the FE of the gaseous product i. z_i is the number of electrons transferred to form the corresponding gaseous product (for CH_4, Z_i is 8). F is Faraday's constant, 96,485 (C mol^{-1}). F_m is the molar flow rate of the gas stream (mol s^{-1}). I is the total current applied (A) and x_i is the mole fraction of the gas product i during the reduction step.

The operation of the cell was carried out with two distinct steps: reduction and oxidation. During the oxidation step, no gaseous product is formed. As the reduction–oxidation cycle goes on, the amount of gaseous product produced is diluted continuously by the CO_2 during the oxidation cycle. In addition, the flow of the catholyte to the cell was kept constant during the oxidation step. Thus, in comparison with the continuous reduction operation, the reduction–oxidation operation generates the gas product that has the mole fraction as follows:

$$x_i = x_i' \times \frac{\Delta t_\mathrm{r} + \Delta t_\mathrm{o}}{\Delta t_\mathrm{r}} \quad (2)$$

where x_i' is the diluted concentration of the gas product i after mixing with gas products from both reduction and oxidation steps, which is measured by GC. Δt_r and Δt_o are the time of reduction and oxidation steps in each cycle, respectively.

The FE of liquid products was calculated as follows:

$$\mathrm{FE}_k = \frac{z_k \times \mathrm{F} \times N_k}{I \times t} \times 100\% \quad (3)$$

where FE_k is the FE of the liquid product k and z_k is the number of electrons transferred to form the corresponding liquid product k. F is the Faraday's constant, 96,485 (C mol^{-1}). N_k is the total number of moles of liquid product k (mol). I is the total current applied (A) and t is the total operation time (s).

Characterization

Ex situ X-ray absorption spectroscopy (XAS) measurements were collected at beamline 12-BM of the Advanced Photon Source (APS) at Argonne National Laboratory. X-ray photoelectron spectroscopy (XPS) was conducted on a Thermo Scientific NEXSA G2 XPS spectrometer equipped with an Al K alpha radiation source and electron flood-gun at a pressure of 8×10^{-8} mbar with a pass energy of 50 eV. All spectra were calibrated with the C 1*s* peak at 284.8 eV. Scanning electron microscopy (SEM) images and SEM-energy dispersive spectroscopy (SEM-EDS) analysis of the samples before and after the different electrocatalytic conditions were measured using FEI Magellan 400.

The operando electrochemical surface-enhanced Raman spectroscopy measurements were carried out using a PGSTAT204 electrochemical workstation coupled with a RENISHAW inVia confocal Raman microscope. The wavelength utilized in the experiment was 633 nm. A custom-designed Raman cell was employed, featuring a platinum wire as the counter electrode and an Ag/AgCl electrode as the reference electrode. A 200-nm layer of Ag was deposited onto a polytetrafluoroethylene (PTFE) substrate using a sputter coater to serve as the working electrode. Electrochemical experiments were conducted in a CO_2-saturated 0.3 M $KHCO_3$ aqueous electrolyte, with the optional addition of Cu^{2+} ions and/or pyridine as specified.

In situ XAS of Cu K edges was performed at the Australian Synchrotron (ANSTO) in operational mode 2. Cu K-edge spectra were recorded with Si(111) monochromators and focusing optics. Data were collected in fluorescence mode using an 18-element solid-state Ge fluorescence detector. XAS data were analysed using Athena software. The in situ XAS was performed in a gas- and liquid-tight spectroelectrochemical cell (SEC) as described in our previous study[48–50]. Ag mesh as substrate was first run in the system, but there was a substantial influence of the Ag on the Cu K-edge signal, which distorted the interpretation of the data. As such, a Sigracet 39 BB carbon paper was used as the electrode, and electrolytes of 0.3 M $KHCO_3$ with and without pyridine containing 3.6 ppm Cu^{2+} were saturated with CO_2 before running experiments. A BioLogic SP-150e single-channel potentiostat was used to control applied potential in a three-electrode configuration. An Ag|AgCl (3 M KCl) reference electrode was used as a reference electrode. A Teflon fabric-reinforced Nafion membrane was used to separate the working and auxiliary chambers.

Studies on the Cu^{2+} concentration in the catholyte were carried out with an iCAP 7400 ICP-OES analyser (Thermo Fisher Scientific). The samples were acidified to below a pH of 2 by H_2SO_4 before the analysis.

Multiphysics modelling

A one-dimensional multiphysics model was developed and previously validated[39] to replicate the experimental conditions. The domain simulated was the cathode catalyst layer and the cation exchange layer (CEL) of the bipolar membrane. The physics considered were species diffusion and electromigration, electrokinetic reaction evolution, bulk buffer reactions, liquid-to-gas phase transfer and current distribution. The boundary condition at the CEL was a proton flux, while the boundary condition at the catalyst layer was a finite flux of electrolyte and a half-cell potential from 0 to −2.5 V. The CEL was modelled with a fixed negative space charge, which limits anion transport due to repulsion. Two electrokinetic reactions were considered: the methane evolution reaction and the hydrogen evolution reaction (HER). To calculate the limiting current density, the HER was disabled. The model was solved using COMSOL Multiphysics version 6.3. Additional details of model parameters can be found in the 'open matrix' case of our previous work[39].

Data availability

All the data supporting the findings of this study are available within the article and its Supplementary Information and Source Data file. Source data are provided with this paper.

References

1. Kibria, M. G. et al. Electrochemical CO_2 reduction into chemical feedstocks: from mechanistic electrocatalysis models to system design. *Adv. Mater.* **31**, 1807166 (2019).
2. Belsa, B. et al. Materials challenges on the path to gigatonne CO_2 electrolysis. *Nat. Rev. Mater.* **9**, 535–549 (2024).
3. Wu, Y. et al. Heterogeneous electrocatalysis of carbon dioxide to methane. *Methane* **2**, 148–175 (2023).
4. Medina, O. E., Amell, A. A., López, D. & Santamaría, A. Comprehensive review of nickel-based catalysts advancements for CO_2 methanation. *Renew. Sustain. Energy Rev.* **207**, 114926 (2025).
5. Liu, Z. H. et al. Recent advances in thermal catalytic CO_2 methanation on hydrotalcite-derived catalysts. *Fuel* **321**, 124115 (2022).
6. Wang, R. & Jin, S. Flexible participation of electrosynthesis in dynamic electricity markets. *Nat. Energy* **9**, 1062–1063 (2024).
7. Samu, A. A. et al. Intermittent operation of CO_2 electrolyzers at industrially relevant current densities. *ACS Energy Lett.* **7**, 1859–1861 (2022).

8. Zhang, H., Liang, Q. & Xie, K. How to rationally design homogeneous catalysts for efficient CO_2 electroreduction? *iScience* **27**, 108973 (2024).
9. Xue, Y., Guo, Y., Cui, H. & Zhou, Z. Catalyst design for electrochemical reduction of CO_2 to multicarbon products. *Small Methods* **5**, 2100736 (2021).
10. Zhu, S. et al. Recent advances in catalyst structure and composition engineering strategies for regulating CO_2 electrochemical reduction. *Adv. Mater.* **33**, 2005484 (2021).
11. Chen, J. & Wang, L. Effects of the catalyst dynamic changes and influence of the reaction environment on the performance of electrochemical CO_2 reduction. *Adv. Mater.* **34**, 2103900 (2022).
12. Lai, W., Qiao, Y., Wang, Y. & Huang, H. Stability issues in electrochemical CO_2 reduction: recent advances in fundamental understanding and design strategies. *Adv. Mater.* **35**, 2306288 (2023).
13. Lee, S. H. et al. Oxidation state and surface reconstruction of Cu under CO_2 reduction conditions from in situ X-ray characterization. *J. Am. Chem. Soc.* **143**, 588–592 (2021).
14. Vavra, J., Shen, T.-H., Stoian, D., Tileli, V. & Buonsanti, R. Real-time monitoring reveals dissolution/redeposition mechanism in copper nanocatalysts during the initial stages of the CO_2 reduction reaction. *Angew. Chem. Int. Ed.* **60**, 1347–1354 (2021).
15. Grosse, P. et al. Dynamic transformation of cubic copper catalysts during CO_2 electroreduction and its impact on catalytic selectivity. *Nat. Commun.* **12**, 6736 (2021).
16. Tomc, B. et al. Deactivation of copper electrocatalysts during CO_2 reduction occurs via dissolution and selective redeposition mechanism. *J. Mater. Chem. A* **13**, 4119–4128 (2025).
17. Lee, S. H. et al. Structural transformation and degradation of Cu oxide nanocatalysts during electrochemical CO_2 reduction. *J. Am. Chem. Soc.* **147**, 6536–6548 (2025).
18. Li, F. et al. Interplay of electrochemical and electrical effects induces structural transformations in electrocatalysts. *Nat. Catal.* **4**, 479–487 (2021).
19. Okatenko, V. et al. Alloying as a strategy to boost the stability of copper nanocatalysts during the electrochemical CO_2 reduction reaction. *J. Am. Chem. Soc.* **145**, 5370–5383 (2023).
20. Zhang, Z. et al. 'Two ships in a bottle' design for Zn–Ag–O catalyst enabling selective and long-lasting CO_2 electroreduction. *J. Am. Chem. Soc.* **143**, 6855–6864 (2021).
21. Ko, Y.-J. et al. Exploring dopant effects in stannic oxide nanoparticles for CO_2 electro-reduction to formate. *Nat. Commun.* **13**, 2205 (2022).
22. Tan, X. et al. Stabilizing copper by a reconstruction-resistant atomic Cu–O–Si interface for electrochemical CO_2 reduction. *J. Am. Chem. Soc.* **145**, 8656–8664 (2023).
23. Levchenko, T. I. et al. Electrocatalytic CO_2 reduction with atomically precise Au_{13} nanoclusters: effect of ligand shell on catalytic performance. *ACS Catal.* **14**, 4155–4163 (2024).
24. Kim, J.-Y. et al. Quasi-graphitic carbon shell-induced Cu confinement promotes electrocatalytic CO_2 reduction toward C_{2+} products. *Nat. Commun.* **12**, 3765 (2021).
25. Thevenon, A., Rosas-Hernández, A., Peters, J. C. & Agapie, T. In-situ nanostructuring and stabilization of polycrystalline copper by an organic salt additive promotes electrocatalytic CO_2 reduction to ethylene. *Angew. Chem. Int. Ed.* **58**, 16952–16958 (2019).
26. Han, Z. et al. Steering surface reconstruction of copper with electrolyte additives for CO_2 electroreduction. *Nat. Commun.* **13**, 3158 (2022).
27. Guntern, Y. T. et al. Nanocrystal/metal–organic framework hybrids as electrocatalytic platforms for CO_2 conversion. *Angew. Chem. Int. Ed.* **58**, 12632–12639 (2019).
28. Guo, S.-T. et al. Stabilizing undercoordinated Zn active sites through confinement in CeO_2 nanotubes for efficient electrochemical CO_2 reduction. *Angew. Chem. Int. Ed.* **63**, e202314099 (2024).
29. Xue, J. et al. Turning copper into an efficient and stable CO evolution catalyst beyond noble metals. *Nat. Commun.* **15**, 5998 (2024).
30. Albertini, P. P. et al. Hybrid oxide coatings generate stable Cu catalysts for CO_2 electroreduction. *Nat. Mater.* **23**, 680–687 (2024).
31. Xu, Y. et al. Low coordination number copper catalysts for electrochemical CO_2 methanation in a membrane electrode assembly. *Nat. Commun.* **12**, 2932 (2021).
32. Chen, S. et al. Engineering water molecules activation center on multisite electrocatalysts for enhanced CO_2 methanation. *J. Am. Chem. Soc.* **144**, 12807–12815 (2022).
33. Fan, Q. et al. Manipulating Cu nanoparticle surface oxidation states tunes catalytic selectivity toward CH_4 or C_{2+} products in CO_2 electroreduction. *Adv. Energy Mater.* **11**, 2101424 (2021).
34. Su, X. et al. Complementary operando spectroscopy identification of in-situ generated metastable charge-asymmetry Cu_2-CuN_3 clusters for CO_2 reduction to ethanol. *Nat. Commun.* **13**, 1322 (2022).
35. Wang, J. et al. In situ X-ray spectroscopies beyond conventional X-ray absorption spectroscopy on deciphering dynamic configuration of electrocatalysts. *Nat. Commun.* **14**, 6576 (2023).
36. Du, Z.-Y. et al. In situ Raman spectroscopic studies of electrochemical CO_2 reduction on Cu-based electrodes. *J. Phys. Chem. C* **128**, 11741–11755 (2024).
37. Zhan, C. et al. Key intermediates and Cu active sites for CO_2 electroreduction to ethylene and ethanol. *Nat. Energy* **9**, 1485–1496 (2024).
38. Du, Z.-Y. et al. Promoting water activation via molecular engineering enables efficient asymmetric C–C coupling during CO_2 electroreduction. *J. Am. Chem. Soc.* **146**, 32870–32879 (2024).
39. Obasanjo, C. A. et al. High-rate and selective conversion of CO_2 from aqueous solutions to hydrocarbons. *Nat. Commun.* **14**, 3176 (2023).
40. Lee, G. et al. CO_2 electroreduction to multicarbon products from carbonate capture liquid. *Joule* **7**, 1277–1288 (2023).
41. Singh, D. P., Ojha, A. K. & Srivastava, O. N. Synthesis of different $Cu(OH)_2$ and CuO (nanowires, rectangles, seed-, belt-, and sheetlike) nanostructures by simple wet chemical route. *J. Phys. Chem. C* **113**, 3409–3418 (2009).
42. Bowmaker, G. A. et al. Mechanochemical synthesis in copper(ii) halide/pyridine systems: single crystal X-ray diffraction and IR spectroscopic studies. *Dalton Trans.* **40**, 5102–5115 (2011).
43. Satyanarayan, P. in *Pyridine: A Useful Ligand in Transition Metal Complexes* (ed. Parashar, P. P.) Ch. 5 (IntechOpen, 2018).
44. Tian, Z.-Q. & Ren, B. Adsorption and reaction at electrochemical interfaces as probed by surface-enhanced raman spectroscopy. *Annu. Rev. Phys. Chem.* **55**, 197–229 (2004).
45. Petrov, K. V. et al. Bipolar membranes for intrinsically stable and scalable CO_2 electrolysis. *Nat. Energy* **9**, 932–938 (2024).
46. Blommaert, M. A. et al. Insights and challenges for applying bipolar membranes in advanced electrochemical energy systems. *ACS Energy Lett.* **6**, 2539–2548 (2021).
47. Nourmohammadi Khiarak, B. et al. Macro- and nano-porous ag electrodes enable selective and stable aqueous CO_2 reduction. *Small* **21**, 2409669 (2025).
48. King, H. J. et al. Photon-induced, timescale, and electrode effects critical for the in situ X-ray spectroscopic analysis of electrocatalysts: the water oxidation case. *J. Phys. Chem. C* **123**, 28533–28549 (2019).

49. Ramadhany, P. et al. Triggering C–N coupling on metal oxide nanocomposite for the electrochemical reduction of CO_2 and NO_x– to formamide. *Adv. Energy Mater.* **14**, 2401786 (2024).
50. Tran-Phu, T. et al. Understanding the role of (W, Mo, Sb) dopants in the catalyst evolution and activity enhancement of Co_3O_4 during water electrolysis via in situ spectroelectrochemical techniques. *Small* **19**, 2208074 (2023).

Acknowledgements

C.-T.D. acknowledges the financial support from the Canada Research Chairs Program, the Natural Sciences and Engineering Research Council of Canada (NSERC), Canada Foundation for Innovation (CFI) and Queen's University. V.G. and F.P.G.d.A. are thankful to PID2022-138127NA-I00 and CEX2019-000910-S (MCIN/AEI/10.13039/501100011033), Fundació Cellex, Fundació Mir-Puig, Generalitat de Catalunya through CERCA and the European Union (NASCENT, 101077243). G.T.S.T.d.S. acknowledges funding from FAPESP (#2023/10268-2 and #2013/07296-2). This research used resources of the Advanced Photon Source (beamline 12-BM), a US Department of Energy (DOE) Office of Science User Facilities, operated for the DOE Office of Science by Argonne National Laboratory under contract number DE-AC02-06CH11357 and the Australian Synchrotron part of ANSTO via proposal M23234. R.K.H. is grateful for an Australian research council future fellowship FT230100054.

Author contributions

C.-T.D. and E.H.S. supervised the project. G.G., B.N.K., C.A.O. and C.-T.D. designed all experiments. G.G., B.N.K., C.A.O. and H.D.T.L. conducted the experiments and data processing. H.L., J.L., Z.Z. and S.L. performed ex situ XAS analysis. H.L. and J.W. performed XPS analysis. H.L. and H.Z. performed in situ Raman analysis. T.T.-P. and R.K.H. performed in situ XAS experiments and analyses. G.T.S.T.d.S., G.G., B.N.K., V.G. and F.P.G.d.A. performed SEM analysis. J.C. performed multiphysics modelling. G.G., B.N.K., H.L., C.A.O. and H.D.T.L. wrote the draft of the manuscript. All authors discussed the results and assisted during manuscript preparation.

Competing interests

The authors declare no competing interests.

Additional information

Supplementary information The online version contains supplementary material available at https://doi.org/10.1038/s41560-025-01883-w.

Correspondence and requests for materials should be addressed to Edward H. Sargent or Cao-Thang Dinh.

Peer review information *Nature Energy* thanks Maximilian Fleischer, Chanyeon Kim and the other, anonymous, reviewer for their contribution to the peer review of this work.